


## Elastic interactions of plastic events in strained amorphous solids before yield

J. Duan, Y. J. Wang, L. H. Dai, and M. Q. Jiang \*

*State Key Laboratory of Nonlinear Mechanics, Institute of Mechanics, Chinese Academy of Sciences,  
Beijing 100190, People's Republic of China  
and School of Engineering Science, University of Chinese Academy of Sciences,  
Beijing 101408, People's Republic of China*



(Received 23 September 2022; accepted 23 November 2022; published 3 January 2023)

It has been widely accepted that the plastic events of amorphous solids after mechanical yield belong to a highly correlated avalanche state. However, whether the plastic events before yield are correlated or not is still unsettled, leaving their interactions largely unexplored. In this paper, by means of atomistic simulations, typical  $\text{Cu}_{50}\text{Zr}_{50}$  metallic glasses, as the model system, are sheared under athermal quasistatic limit to study these plastic events. The statistical analysis of both stress drops and waiting times reveals that plastic events before yield are in the correlated avalanche state and the interactions among them are mediated by the robust elasticity. The temporal correlation analysis of the nonaffine displacement fields further reveals that the elastic interactions are short-lived strong but long-standing weak, which results in the fractal morphology of potential energy landscape. By introducing vibrational modes to explore plastic events, we clearly exhibit the way how the elastic interactions organize the Eshelby-type shear transformations into avalanched plastic events. The correlation matrix, with its component being the dot product of the vibrational modes at different configurations, is defined to trace the evolution of vibrational modes during elastic deformation and across plastic events. Three reasons accounting for the robust elasticity are identified: (i) the limited destruction of plastic events on global elasticity, (ii) the persistent hard spots embedded in elastic matrix, and (iii) the self-recovery of elastic matrix during elastic deformation. Our results clarify the atomic-scale nature of both elastic deformation and plastic instabilities before yield in amorphous solids, providing fundamental information for the development of elastoplastic constitutive models.

DOI: [10.1103/PhysRevMaterials.7.013601](https://doi.org/10.1103/PhysRevMaterials.7.013601)

### I. INTRODUCTION

Amorphous solids are ubiquitous in nature and technology, ranging from obsidian, colloidal, and metallic glasses, to granular materials. Unlike ordered solids or crystals residing in the global energy minimum, long-range disordered amorphous solids have complex rugged potential-energy landscape (PEL) with hierarchical or fractal local minima [1–3]. Upon external perturbations, such PEL responses have a wide spectrum of vibrations or activations, consequently giving rise to a series of plastic events that occur at different spatiotemporal scales. Considerable efforts have been spent in the past decades to demystify these sophisticated events, and thus to construct constitutive laws for amorphous plasticity along mean-field or mesoscale lines [4–11].

In amorphous solids, smallest component units of plastic events have been identified as Eshelby-type shear transformations (STs) that are local cooperative rearrangements. These events will incur elastic perturbations around them, which in turn trigger other events. Via such nonlocal elasto-plastic interactions, STs can organize into the plastic events operating on multiple scales in both time and space. Close to mechanical yield or in the postyield regime, plastic events

have been extensively studied [12–25], from which some important knowledge can be gleaned. First, most events belong to a highly correlated avalanche state, as the probability distribution of the stress or energy drops released by avalanches exhibits the universal power-law decay with the self-similar character. Second, these avalanched events are extended, representing metabasin-to-metabasin transitions on PEL, and the avalanche sizes in general scale as the system sizes with a fractal link. Third, the irreversible plastic events dominate the mechanical response of the system after yield, whereas event-induced elastic fields are dynamically transient in time. In other words, the interaction between plastic events after yield is transiently elastic.

It is intriguing that plastic events can be detected in the apparently linear elastic stage much below the plastic yield. Conventionally, such events are considered to be rare, highly localized, and thus spatiotemporally uncorrelated. Since a very limited number of STs are involved, they are often taken as the touchstone of various predictors for amorphous plasticity [26–36]. On the other hand, however, the statistics of plastic events even at very small strains far below yield still points to so-called elastic avalanches [37,38], but with a power-law exponent ( $\sim 1.0$ ) very different from that ( $\sim 1.5$ ) obtained in the steady-state flow regime. The underlying physics is suggested to result from the marginally stable state of metabasins with a hierarchy of fine basins [3,39,40].

\*mqjiang@imech.ac.cn

Under small strain perturbations, the elastic avalanches are caused by self-organized basin-to-basin transitions but within the initial metabasin. Thus, whether the plastic events before yield are avalanched or not is still under debate and their interactions are *a fortiori* unknown. In this work, we focus on these across-basin events, because they bridge the gap between fundamental STs and macroscopic plastic response such as plastic yield [11,21,36,41–43] and shear banding [25,44–47].

Meanwhile, the situation that plastic events exist deep in the elastic regime calls into question the existence of elasticity of amorphous solids with some puzzles or anomalies [39,48–51]. It is well accepted that solids in the continuum limit can be approximated as a homogeneous elastic body, in which low-frequency vibrational modes are extended phonons that can be treated as linear elastic waves and follow the Debye law. However, for all amorphous solids, the continuum limit of their vibrational modes no longer follows the Debye law [52–55], and instead there appear some localized modes that follow another universal non-Debye scaling law [56–61]. More interestingly, some critical modes can evolve from these low-frequency extended or localized modes to fingerprint upcoming plastic events in the amorphous structure. It therefore provides an efficient way to clarify the states and correlations of plastic events by analyzing the event-associated vibrational modes. In a recent work by some of us [62], the strain evolution of low-frequency modes associated with the first four ST events was carefully traced, preliminarily revealing strong, elastic interactions among the neighboring events. But, the universality and generality of such interactions urgently needs further exploration by examining more plastic events beyond pure STs.

In this paper, we aim to answer these questions: Are the plastic events before yield correlated or not? And if yes, how do they interact with each other? By means of molecular dynamic (MD) simulations, prototypical three-dimensional (3D) Cu-Zr metallic glasses are selected as our model system to study the plastic events of strained amorphous solids before yield. By the statistical analysis of stress drops and waiting times, we find that plastic events are in the avalanche state and their interactions are mediated by the robust elasticity. The temporal correlation analysis of nonaffine displacement fields further indicates that these interactions are strong in the short term, but weak in the long term. Finally, vibrational modes, as the manifestation of transient elasticity in the vibrational space, are studied to reveal how the interactions are mediated by elasticity and why the elastic media are robust.

The paper is organized as follows. Section II gives the detailed protocol of the sample preparation and mechanical loading. Section III presents the theoretical description of the deformation dynamics of athermal quasistatic (AQS) amorphous system. In Sec. IV, the statistical analysis of stress drops and waiting times determines whether the plastic events are correlated or not. In Sec. V, the evolution of the elastic interactions between plastic events is revealed by the temporal correlation analysis of the nonaffine displacement fields. In Sec. VI, vibrational modes are introduced to explore the way and cornerstone of these interactions. At last, some conclusions and discussion are highlighted in Sec. VII.

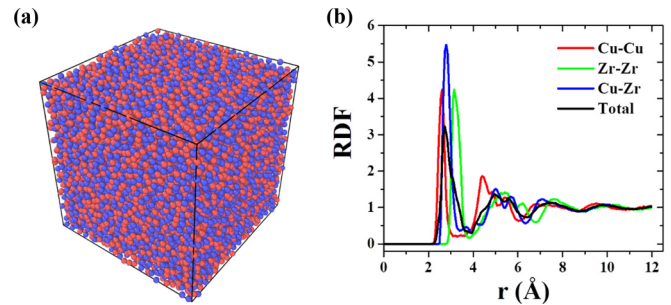


FIG. 1. Atomic model of  $\text{Cu}_{50}\text{Zr}_{50}$  metallic glass: (a) the 3D packing configuration; (b) the radial distribution function.

## II. ATOMISTIC MODELING

### A. Sample preparation

A prototypical  $\text{Cu}_{50}\text{Zr}_{50}$  model metallic glass is adopted as a representative of general amorphous solids. The structure and property of this binary glass have been well studied previously by us [54,63–66]. The present model herein contains 19 652 particles interacting with the Finnis-Sinclair-type embedded-atom method potential [67]. During the sample preparation and the mechanical loading processes, periodic boundary conditions are applied on all three dimensions. All atomistic simulations are performed using the LAMMPS code.

We prepare the glass sample from its melting state, which has been equilibrated at 2000 K for 2 ns that is much longer than its  $\alpha$ -relaxation time. Then, the equilibrated liquid is quenched to 0 K with a cooling rate of  $10^{10}$  K/s. An additional sub- $T_g$  annealing during the cooling process is performed at 700 K for 60 ns to accelerate the aging dynamics, which drives the inherent structure (IS) to the deeper basin on PEL [68]. After being quenched to 0 K, the sample is additionally in-depth relaxed to a local potential-energy minimum by conjugate gradient algorithm. During the sample preparation process, the external pressure maintains at zero. The temperature and pressure are controlled with Nosé-Hoover thermostat and Parrinello-Rahman barostat, respectively. Figure 1(a) shows a typical sample with the 3D packing configuration of  $\sim 7 \times 7 \times 7 \text{ nm}^3$ . The amorphous nature of this sample is confirmed by the radial distribution function as shown in Fig. 1(b). Except for the short-to-medium-range order, there is a clear long-range disorder beyond  $\sim 1 \text{ nm}$ . One can notice a split of second peaks which indicates a typical feature of the glassy solid.

### B. Athermal quasistatic shear

AQS shear is adopted as our loading protocol to gather plastic events. This loading protocol has been widely used to study the deformation behavior of amorphous solids ranging from metallic glasses to simple pairwise-potential glasses [18,69,70]. The AQS algorithm consists of two repeated alternating steps: (i) Apply an affine simple shear deformation to the sample with a very small strain step  $\delta\gamma = 1 \times 10^{-5}$ ; (ii) Minimize the potential energy of the sample with the fixed simulation box by conjugate gradient algorithm. In this protocol, the glass configuration during deformation process always resides in an IS and the plastic events are induced by

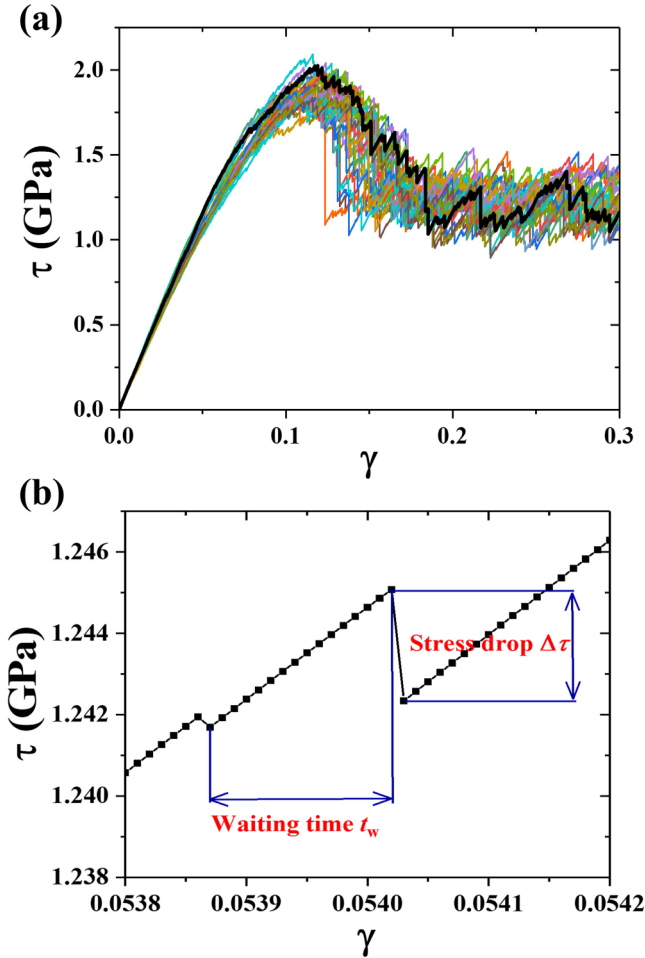


FIG. 2. (a) Thirty stress-strain curves of five independent samples sheared in six different directions. The black thick one belongs to the selected representative sample. (b) A partial magnification of the black thick curve in (a). The curve consists of plastic events and elastic portions, which are quantitatively characterized by stress drops and waiting times, respectively.

shear strain, not by thermal activation. Therefore, the AQS shear captures the plastic instabilities of athermal amorphous solids, whose role is still crucial for thermal glasses in the finite temperature and strain rate [15].

In order to obtain sufficient plastic events for statistical analyses in Sec. IV, five independent samples are prepared and each of the samples is then sheared along six different directions, viz.,  $\pm xy$ ,  $\pm yz$ , and  $\pm xz$ . But, a representative sample sheared along the  $+xy$  direction is selected for the analyses of nonaffine displacements in Sec. V and vibrational modes in Sec. VI to save the computing expense. Figure 2(a) shows the 30 stress-strain curves in total and the black thick curve belongs to the selected representative sample. The extended and avalanched plastic events after yield, associated with large stress drops, inhibit the increase of macroscopic shear stress, leading to the steady-state flow state. In contrast, the plastic events before yield are smaller and more localized, which give rise to the slight deviation of mechanical response from standard linear elasticity. These small events are clearly shown by the partial magnification of stress-strain

curve in Fig. 2(b). The elastic deformation is interrupted by intermittent plastic events, shown as discrete stress drops on the stress-strain curve. Each event is complete in an individual strain step. Therefore, the mechanical response of amorphous solids under AQS condition can be clearly divided into two parts: plastic events and elastic portions. A plastic event corresponds to a stress discontinuity on the stress-strain curve and an elastic portion is the region between two adjacent plastic events. The plastic event and the elastic portion can be quantitatively characterized by the stress drop  $\Delta\tau$  (stress reduction of the plastic event) and the waiting time  $t_w$  (strain interval of the elastic portion), respectively. The alternately interspersed plastic events and elastic portions, corresponding to the dissipation and accumulation of elastic energy, constitute the whole deformation process.

### III. DEFORMATION DYNAMICS OF AQS AMORPHOUS SYSTEM

Under the AQS condition, the plastic instability of amorphous solids is a saddle-node bifurcation process (a minimum in PEL hits a saddle) induced by applied strain [71,72]. To describe the process from the perspective of the structure of PEL, Maloney and Lemaître have constructed the decomposition of deformation in vibrational space [72,73], which is given in the following for the completeness of the description.

A 3D amorphous system of  $N$  particles under AQS simple shear is taken into consideration. The system's configuration is represented by the position of all particles in the reference state  $\mathbf{r}$ , which is a  $3N$ -dimensional vector. The 3D vector  $\mathbf{r}^i$ , denoting the position of particle  $i$ , is the component of  $\mathbf{r}$  on particle  $i$ . The AQS system is constrained to follow the deformation-induced changes of IS, so the configuration  $\mathbf{r}$  is only determined by the applied shear strain  $\gamma$ , that is,  $\mathbf{r}(\gamma)$ . The total potential energy  $U$  is a function of the system's configuration  $\mathbf{r}(\gamma)$  and the applied shear strain  $\gamma$ , that is,  $U(\mathbf{r}(\gamma), \gamma)$ . According to the mechanical equilibrium condition, we have

$$\frac{\partial U}{\partial \mathbf{r}} = \mathbf{0}. \quad (1)$$

Besides, the stability of IS during elastic deformation leads to the continuous trajectory in configuration space. In other words,  $\mathbf{r}(\gamma)$  is a continuous function of strain  $\gamma$ . Taking the total derivative of Eq. (1) to  $\gamma$ , we further have

$$\frac{\partial^2 U}{\partial \mathbf{r} \partial \mathbf{r}} \cdot \frac{d\mathbf{r}}{d\gamma} + \frac{\partial^2 U}{\partial \mathbf{r} \partial \gamma} = \mathbf{0}. \quad (2)$$

We reduce vector  $\mathbf{r}$  by particles' mass and get a  $3N$ -dimensional vector  $\mathbf{R}$ .  $\mathbf{R}^i$  is the component of  $\mathbf{R}$  on particle  $i$ , and it is related with  $\mathbf{r}^i$  by

$$\mathbf{R}^i = \sqrt{m_i} \cdot \mathbf{r}^i, \quad (3)$$

where  $m_i$  is the mass of particle  $i$ . Then, Eq. (2) can be rewritten as

$$\frac{\partial^2 U}{\partial \mathbf{R} \partial \mathbf{R}} \cdot \frac{d\mathbf{R}}{d\gamma} + \frac{\partial^2 U}{\partial \mathbf{R} \partial \gamma} = \mathbf{0}. \quad (4)$$

Equation (4) includes the dynamical Hessian matrix:

$$\mathbf{H} = \frac{\partial^2 U}{\partial \mathbf{R} \partial \mathbf{R}}, \quad (5)$$

and the nonaffine force field:

$$\mathbf{\Xi} = -\frac{\partial^2 U}{\partial \mathbf{R} \partial \gamma}. \quad (6)$$

Hessian matrix  $\mathbf{H}$  contains the vibrational information of system, and its eigenvalues and eigenvectors correspond to the square of vibrational frequencies  $\omega_p^2$  and vibrational modes  $\Psi_p$ , respectively. Nonaffine force field  $\mathbf{\Xi}$  represents the nonequilibrium forces on particles after applying a small affine shear strain to the system. The existence of these nonequilibrium forces results in the nonaffine displacements during elastic deformation, which contributes to the computation of elastic constants. Substituting Eqs. (5) and (6) into Eq. (4), we have

$$\mathbf{H} \cdot \frac{d\mathbf{R}}{d\gamma} = \mathbf{\Xi}. \quad (7)$$

Inverting the Hessian matrix  $\mathbf{H}$  and decomposing the nonaffine force field  $\mathbf{\Xi}$  on vibrational modes  $\Psi_p$ , the analytical expression of elastic deformation that decomposes in the vibrational space is obtained:

$$\frac{d\mathbf{R}}{d\gamma} = \mathbf{H}^{-1} \cdot \mathbf{\Xi} = \left( \sum_p \frac{\Psi_p \Psi_p}{\omega_p^2} \right) \cdot \mathbf{\Xi} = \sum_p \left( \frac{\mathbf{\Xi} \cdot \Psi_p}{\omega_p^2} \Psi_p \right). \quad (8)$$

The projection coefficient of elastic deformation  $d\mathbf{R}/d\gamma$  on vibrational mode  $\Psi_p$  is  $(\mathbf{\Xi} \cdot \Psi_p)/\omega_p^2$ , where the numerator  $\mathbf{\Xi} \cdot \Psi_p$  and denominator  $\omega_p^2$  are the motivation and resistance of the nonaffine elastic deformation in the direction of vibrational mode  $\Psi_p$ , respectively. However, Eq. (8) breaks down for plastic deformation. This is because  $\mathbf{r}(\gamma)$  is no longer a continuous function of the strain  $\gamma$  at the strain point where plastic instability occurs. Nevertheless, Eq. (8) still provides much useful information for understanding the plastic deformation. When approaching plastic instability, the frequency of the lowest-frequency mode, excluding the three Goldstein modes with zero frequency, tends to zero and the corresponding projection coefficient diverges. This indicates that plastic instability is signified by the lowest frequency going to zero. Correspondingly, the initial instability path is guided by this critical mode with zero frequency. Thus, the vibrational modes approaching instability provide a set of base directions for exploring the deformation path of plastic events on PEL.

In atomistic simulations, the obtained configurations  $\mathbf{r}(\gamma)$  come from discrete strain points that are the integer multiples of strain step  $\delta\gamma = 1 \times 10^{-5}$ . The component of mass-reduced nonaffine displacements on particle  $i$  between configurations  $\mathbf{r}(\gamma')$  and  $\mathbf{r}(\gamma'')$  can be expressed as

$$\Delta \mathbf{R}^i(\gamma', \gamma'') = \sqrt{m_i} \cdot \Delta \mathbf{r}^i(\gamma', \gamma'') = \sqrt{m_i} \cdot (\mathbf{r}^i(\gamma'') - \mathbf{r}^i(\gamma')), \quad (9)$$

where  $\mathbf{r}^i(\gamma')$  and  $\mathbf{r}^i(\gamma'')$  are, respectively, the position of particle  $i$  at shear strain  $\gamma'$  and  $\gamma''$  in reference configuration

$\mathbf{r}(\gamma')$ . Then, the distance between  $\mathbf{r}(\gamma')$  and  $\mathbf{r}(\gamma'')$  in the configuration space can be quantified as

$$\|\Delta \mathbf{R}(\gamma', \gamma'')\| = \left( \sum_{i=1}^N \|\Delta \mathbf{R}^i(\gamma', \gamma'')\|^2 \right)^{1/2}, \quad (10)$$

where  $\|\dots\|$  denotes the 2-norm of a vector. When the configurations  $\mathbf{r}(\gamma')$  and  $\mathbf{r}(\gamma'')$  are, respectively, designated as the beginning and ending strain points of plastic events,  $\|\Delta \mathbf{R}(\gamma', \gamma'')\|$  can measure the magnitude of plastic events and is abbreviated as  $\|\Delta \mathbf{R}_{\text{plastic}}\|$ . The same treatment can be performed for elastic portions, and the associated abbreviation is  $\|\Delta \mathbf{R}_{\text{elastic}}\|$ .

Taking vibrational modes as a set of base directions,  $\Delta \mathbf{R}_{\text{plastic}}$  can be decomposed on vibrational modes at the beginning strain points of plastic events:

$$\frac{\Delta \mathbf{R}_{\text{plastic}}}{\|\Delta \mathbf{R}_{\text{plastic}}\|} = \sum_p \alpha_p \frac{\Psi_p}{\|\Psi_p\|}. \quad (11)$$

However, note that coefficients  $\alpha_p$  are no longer deterministic like elastic deformation, but event dependent, which will be clearly analyzed in Sec. VI A.

## IV. STATISTICAL ANALYSES

### A. Stress drop

Figure 3(a) plots the measured stress drops in 30 stress-strain curves as a function of the applied strain. The stress drops before yield exhibit an approximately linear dependence on the applied stress [74]. Taking this linear dependence into consideration, we normalize the stress drop  $\Delta\tau$  by the stress level  $\tau$  when the stress drop occurs and get a dimensionless parameter called normalized stress drop:

$$S = \frac{\Delta\tau}{\tau}. \quad (12)$$

The normalized stress drops as a function of the applied strain are shown in Fig. 3(b). We can find that the normalized stress drops are small and steady within the strain range of 0–0.1, suggesting that these plastic events are similar to some extent and can be classified into one category. Thus, this strain range, bounded by the vertical dashed line in Fig. 3(b), is chosen to study the plastic events before yield. It is noted that these events are very different from those beyond the strain of 0.1 where the global yield occurs. This critical strain of 0.1 is very close to the yield point of a MD Cu<sub>50</sub>Zr<sub>50</sub> sample determined by the potential energy versus strain method under oscillating shear [75].

We conduct the statistical analyses of the normalized stress drops  $S$  at different deformation stages and the results are shown in Fig. 4. The probability density function of  $S$  shows a power-law distribution with the power-law exponents changing from about 1 in the initial strain range 0–0.02 to about 1.5 in the subsequent strain range 0.02–0.1. The power-law distribution signifies that plastic events occur in the form of avalanches and they are interacted with each other. The avalanched plastic events have been widely found in the postyield region of amorphous solids [12,13,24,76,77], but rarely reported before mechanical yield [38,78–80]. Power-law exponent of 1 suggests that the slightly perturbed system

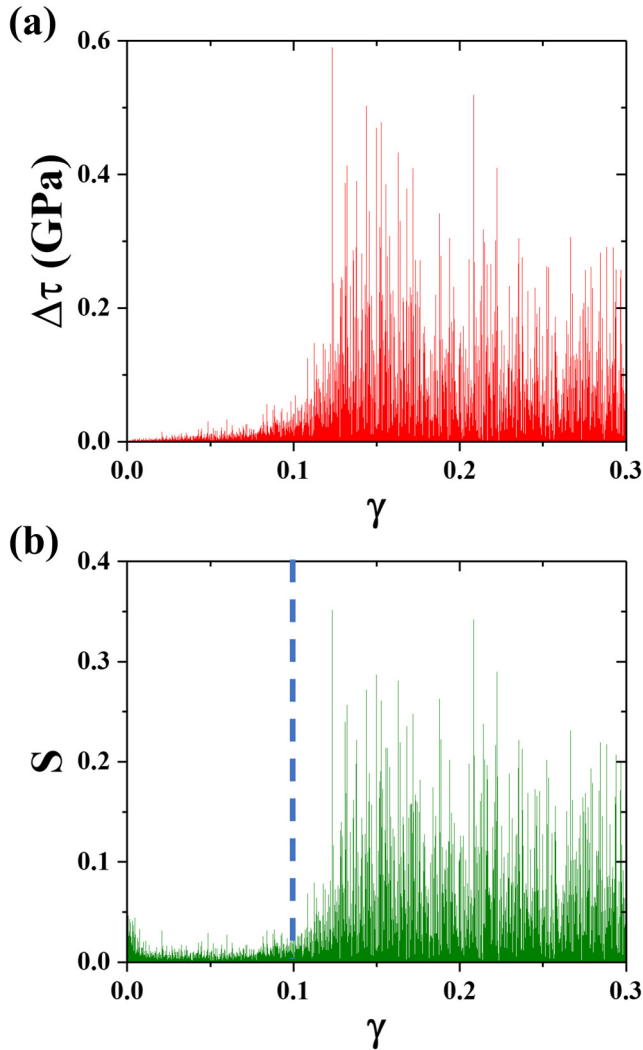


FIG. 3. (a) Stress drops and (b) normalized stress drops in 30 stress-strain curves as a function of the applied strain. The vertical dashed line in (b) indicates the upper limit of the strain range 0–0.1, within which plastic events are studied.

belongs to the marginally stable state where the bottom of the initial metabasin is very rough with a hierarchy of subbasins [3]. This exponent has been predicted by the mean-field theory of marginally stable state in Gardner phase [37] and also observed by the statistics of plastic events at the very small applied strain [38]. In contrast, power-law exponent of 1.5 suggests a typical self-organized criticality [81], which has been universally observed in the steady-state flow regime of various amorphous solids [77,82] and predicted by the mean-field depinning theory [83,84]. The same exponent 1.5 before yield and in steady-flow regime is also observed in the simulation of two-dimensional Lennard-Jones glass under AQS, and the authors ascribe it to the emergence of the criticality with shear loading [79]. Thus, the change of the power-law exponents may suggest a transition from marginally stable state to self-organized critical state, resulting from the gradual rise of the configuration's positions in the initial metabasin caused by mechanical loading.

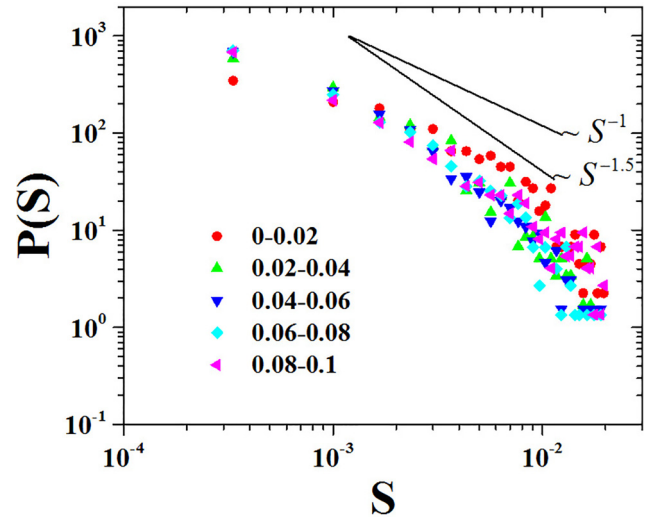


FIG. 4. Probability density function of normalized stress drops at different deformation stages shown by legend. The power-law exponents changes from about 1 in strain range 0–0.02 to about 1.5 in strain range 0.02–0.1 with mechanical loading.

Next, we determine the number of particles involved in these plastic events. The power-law distribution of the normalized stress drops in Fig. 4 indicates that the size of plastic events spans a wide range. It is thus unreasonable to judge whether a particle participates in a plastic event by setting a fixed cutoff of the nonaffine displacements of this particle. Instead, the displacement participation number ( $DPN$ ), based on the localization of the nonaffine displacement fields of the plastic event, is a more reasonable parameter [85], which is defined as

$$DPN = \frac{(\sum_i \|(\Delta \mathbf{R}^i)_{\text{plastic}}\|^2)^2}{\sum_i \|(\Delta \mathbf{R}^i)_{\text{plastic}}\|^4}. \quad (13)$$

$DPN$  ranges from 1 to  $N$ . If  $\Delta \mathbf{R}_{\text{plastic}}$  is concentrated on a single particle, then  $DPN$  equals 1. If  $\Delta \mathbf{R}_{\text{plastic}}$  distributes homogeneously on every particle, then  $DPN$  equals  $N$ . Figure 5 shows the relationship between  $DPN$  and  $\|\Delta \mathbf{R}_{\text{plastic}}\|$ . The increase of  $DPN$  with  $\|\Delta \mathbf{R}_{\text{plastic}}\|$  indicates that larger plastic events contain more particles. The number of particles involved in plastic events ranges from several to several hundreds, shown by the wide range of the values of  $DPN$ . Plastic events contain at least several particles, which is comparable to the lower bound of a ST [41,86]. Many STs organize into the avalanched plastic events by interactions, leading to the plastic events containing several hundreds of particles.

The spatial organization of plastic events is also investigated by the spatial autocorrelation analysis of shear strain field. Figure 6(a) shows the 3D distribution of the cumulative atomic shear strain  $\gamma_{xy}$  within applied strain range of 0–0.1, which indicates that sample deforms homogeneously before yield and plastic events are uniformly dispersed throughout the sample. The 3D spatial autocorrelation function of the cumulative  $\gamma_{xy}$  in Fig. 6(a) is defined as

$$C(\delta \mathbf{r}) = \langle \gamma_{xy}(\mathbf{r}) \gamma_{xy}(\mathbf{r} + \delta \mathbf{r}) \rangle, \quad (14)$$

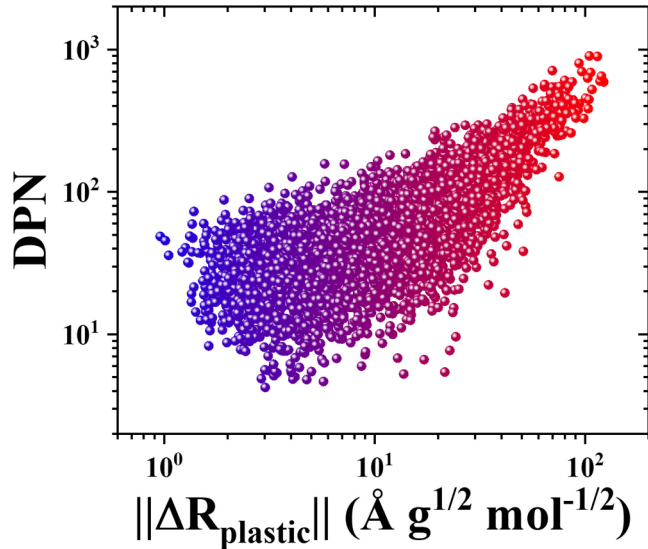


FIG. 5. Relationship between  $DPN$  and  $\|\Delta\mathbf{R}_{\text{plastic}}\|$ .  $DPN$  increases with  $\|\Delta\mathbf{R}_{\text{plastic}}\|$  and has a wide range from several to several hundreds.

where the angle bracket denotes the average over the 3D space. Figure 6(b) shows the  $x$ - $y$  cross section of the calculated  $C(\delta\mathbf{r})$ . We observe an obvious quadrupole pattern that is the typical characteristic of STs embedded in isotropic elastic medium [25,87–89]. However, this pattern shows a

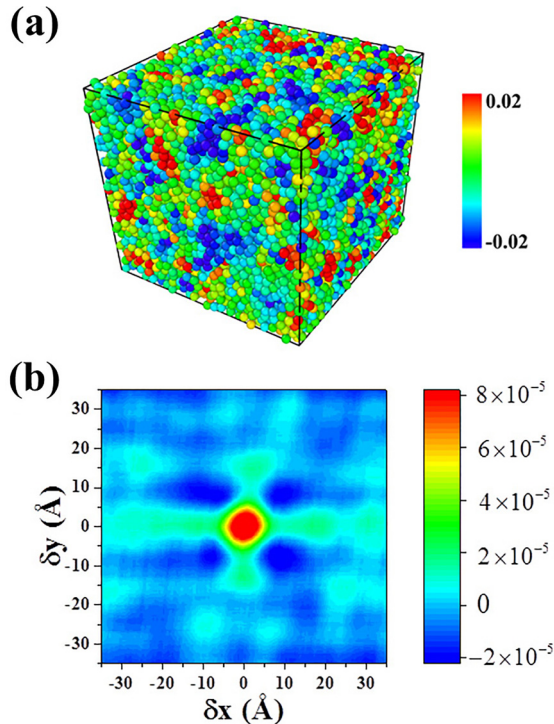


FIG. 6. (a) The 3D spatial distribution of the cumulative atomic shear strain  $\gamma_{xy}$  within strain range 0–0.1. Sample is sheared along  $xy$  direction. (b) Plot of the  $x$ - $y$  cross section of the 3D spatial autocorrelation function of the cumulative atomic shear strain  $\gamma_{xy}$  in (a), exhibiting a characteristic quadrupole pattern.

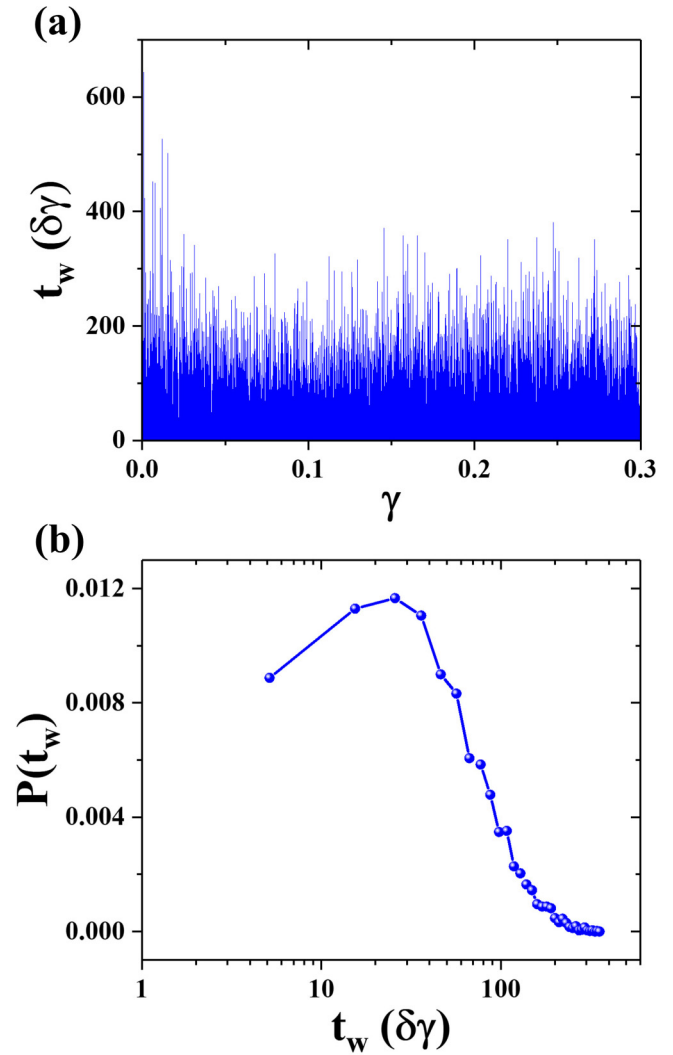


FIG. 7. (a) Waiting times in 30 stress-strain curves as a function of the applied strain. (b) Probability density function of waiting times shows an obvious peak close to 25 strain steps.

preferential correlation along the shear (horizontal) direction. The reason comes from the elastic interactions between these plastic events, which will be discussed in Sec. V.

### B. Waiting time

Figure 7(a) plots the measured waiting times  $t_w$  in 30 stress-strain curves as a function of the applied strain. Different from stress drops [Fig. 3(a)], the waiting times show no obvious dependence on the stress level within strain range of 0–0.1 [74]. The result of the statistical analysis of waiting times is shown in Fig. 7(b). The probability density function of the waiting times shows an obvious peak at  $t_w$  closes to 25 strain steps. The decrease of probability before the peak indicates that the system becomes stable again after the occurrence of a plastic event, which signifies that the system is solidlike and the elasticity is robust [90]. The decrease of probability after the peak results from the instability of the soft spots with mechanical loading. Thus, the appearance of the characteristic peak is the combined effect of the robust

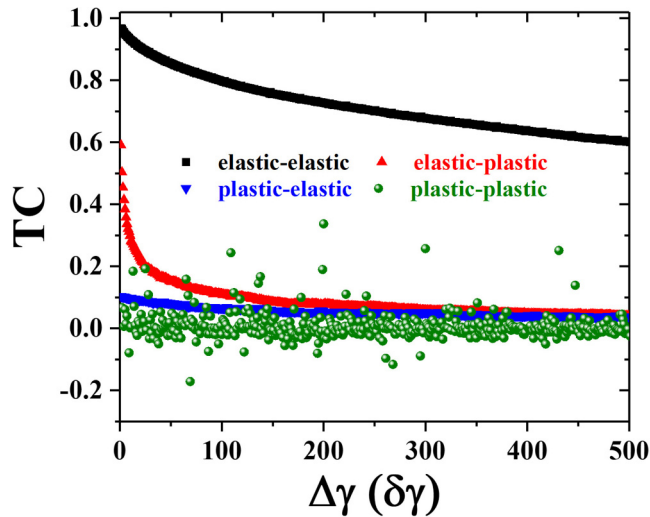


FIG. 8. Correlation function of nonaffine displacement fields as a function of strain interval. There are four categories of curves shown by legend according to the properties of nonaffine displacement fields.

elasticity and the plastic instability. Based on the statistical analyses of stress drops and waiting times, we conclude that the interactions between avalanched plastic events before yield are mediated by the robust elasticity.

## V. NONAFFINE DISPLACEMENTS ANALYSIS

To explore the degree of interactions between plastic events, we conduct the temporal correlation analysis of the nonaffine displacement fields and the correlation function is defined as

$$TC(\Delta\gamma) = \left\langle \frac{\Delta\mathbf{R}_{\text{step}}(\gamma)}{\|\Delta\mathbf{R}_{\text{step}}(\gamma)\|} \cdot \frac{\Delta\mathbf{R}_{\text{step}}(\gamma + \Delta\gamma)}{\|\Delta\mathbf{R}_{\text{step}}(\gamma + \Delta\gamma)\|} \right\rangle, \quad (15)$$

where  $\Delta\mathbf{R}_{\text{step}}(\gamma)$  denotes the nonaffine displacement fields within a strain step, which is short for  $\Delta\mathbf{R}(\gamma, \gamma + \delta\gamma)$ . There are two kinds of the nonaffine displacement fields: one is from the elastic deformation step and the other from the plastic event step. Therefore, the correlation function can be divided into four categories based on the properties of the nonaffine displacement fields of the terms  $\Delta\mathbf{R}_{\text{step}}(\gamma)$  and  $\Delta\mathbf{R}_{\text{step}}(\gamma + \Delta\gamma)$ , which are labeled as elastic-elastic, elastic-plastic, plastic-elastic, and plastic-plastic.  $\langle \dots \rangle$  denotes the average of each category within the applied strain range 0–0.1. The correlation function (15) reflects the spatial similarity of the nonaffine displacement fields separated by strain interval  $\Delta\gamma$  and the results are shown in Fig. 8.

The black curve shows the correlation function between two elastic deformation steps separated by strain interval  $\Delta\gamma$ . With the increase of the strain interval, the correlation decays slowly from about 1 and remains 0.6 when  $\Delta\gamma$  approaches 500 strain steps. The large and slowly decaying correlation indicates that the similarity of the elastic displacement fields is relatively high over a long strain range. This reflects that the elasticity is very robust and the elastic matrix as a skeleton can support the whole deforming system. It is worth noting that as the strain interval increases, two elastic fields would

span several plastic events, but their correlation is still high, which signifies that the destruction of plastic events on elastic matrix is limited. The red curve shows the correlation between the elastic displacement field and the subsequent plastic displacement field. We find that the elastic-plastic correlation value decays rapidly from a high value of nearly 0.6 to below 0.2 at the interval of 30 strain steps. This behavior implies that there exists a short-term strong correlation between the elastic deformation and subsequent plastic event. The correlation between the elastic deformation and the previous plastic events is shown by the blue curve. It has a quite low value below 0.1 and is constantly decaying. The weak correlation makes it difficult to infer previous plastic events based on the current elasticity. In other words, the deforming elastic media has little memory of the plastic events that previously occurred in it. Either the red curve (elastic-plastic) or the blue one (plastic-elastic) does not decay to zero over the studied strain range ( $500\delta\gamma$ ). This long-term weak correlation between elasticity and plasticity also results from the robustness of the elastic matrix before yield. The green points give the correlation between arbitrary two plastic events separated by strain interval  $\Delta\gamma$ . The value of most green points fluctuates around zero, but this does not mean that the plastic events are uncorrelated with each other. It just means that they occur in different locations and manners in 3D space, i.e., their detailed configurations are not spatially similar, which is consistent with the uniform macroscopic deformation before yield.

The underlying picture is that plastic events can stir the elastic environment around them and thus the elastic environment that carries the perturbations of the plastic events will incubate the subsequent plastic events. Therefore, we can draw a conclusion from the results of Fig. 8 that mediated by the robust elasticity, there exist short-term strong interactions and long-term weak interactions among plastic events, although these events are not spatially similar. Furthermore, the elastic-plastic correlation value of the red curve is greater than 0.2 at the strain interval of  $25\delta\gamma$  corresponding to the characteristic waiting time in Fig. 7(b), also indicating that there are relatively strong interactions between adjacent plastic events, which is consistent with our previous work by examining the first four events [62]. The strain interval of most plastic events (not adjacent) before yield is large, so these events are long-term weakly interacted. This explains why the quadrupolar pattern appears in Fig. 6(b).

The AQS deformation of amorphous solids can also be understood by the morphology of PEL. We adopt the nonaffine distance matrix to describe the morphology of PEL and its expression is [77]

$$\chi(\gamma', \gamma'') = \frac{\|\Delta\mathbf{R}(\gamma', \gamma'')\|^2}{N}. \quad (16)$$

As can be seen in Fig. 9(a), the pattern of the calculated  $\chi(\gamma', \gamma'')$  consists of many squares of varying sizes and nodes that connect these squares. Dark blue squares represent the basins within which the ISs are close with each other and the nodes represent the barrier crossing processes. From the lower-left corner to the upper-right corner of the pattern, the squares become smaller and the nodes become denser. This indicates that the system accelerates deformation and surmounts the barrier faster with mechanical loading, which

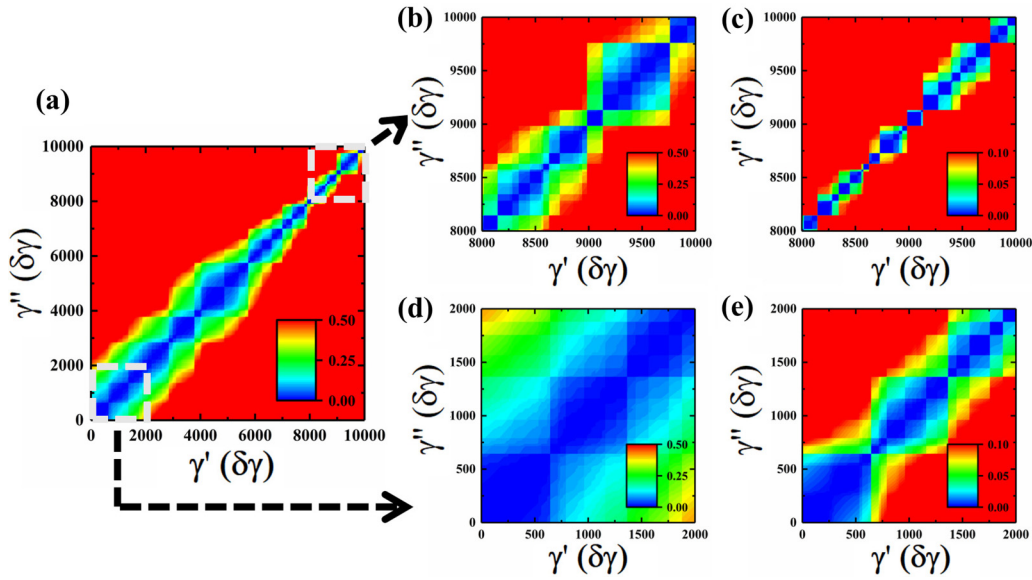


FIG. 9. Nonaffine displacement matrix reflects fractal characteristics of PEL. (a) Nonaffine displacement matrix within the strain range 0–0.1. (b), (d) Magnification of two regions represented by dashed window in (a). (c) and (e) correspond to (b) and (d) with a more precise color scale, respectively.

results from larger plastic events consisting of more STs. Figures 9(b) and 9(d), respectively, show the magnification of the selected regions of dashed window in Fig. 9(a), and the corresponding precise patterns with a smaller color scale are shown in Figs. 9(c) and 9(e). A dark blue square can consist of many smaller squares with similar characteristics, clearly demonstrating that some small basins can organize into a large basin and the morphology of PEL is fractal [3]. The formation of the fractal PEL pattern is consistent with the self-similar avalanched plastic events with a power-law distribution of the normalized stress drops in Fig. 4.

## VI. VIBRATIONAL MODE ANALYSES

From the results in Secs. IV and V, we reveal that the robust elasticity mediates the short-term strong, but long-term weak interactions between plastic events before yield. However, two key questions remain not answered. One is, how does elasticity mediate the interactions between plastic events? The other is, why does elasticity remain robust with the continuous occurrence of plastic events? As theoretically derived in Sec. III, vibrational modes, as the manifestation of transient elasticity in the vibrational space, closely relate to the plastic events. Thus, the two questions should be resolved by exploring the participation of vibrational modes in plastic events (Sec. VIA) and the evolution of vibrational modes in elastic portions and plastic events (Sec. VIB), respectively.

### A. Participation of vibrational modes in plastic events

Firstly, we study the participation of vibrational modes in plastic events. A parameter that is the square of the coefficient  $\alpha_p$  in Eq. (11) is defined to measure the participation degree:

$$PD_p = \alpha_p^2 = \left( \frac{\Delta \mathbf{R}_{\text{plastic}}}{\|\Delta \mathbf{R}_{\text{plastic}}\|} \cdot \frac{\Psi_p}{\|\Psi_p\|} \right)^2. \quad (17)$$

The larger the participation degree, the more the vibrational modes dominate the plastic events. Summation of  $PD_p$  of all modes equals 1 due to the orthogonality of vibrational modes.

Figure 10 shows the calculated participation degree of the vibrational modes of three representative plastic events with different  $\|\Delta \mathbf{R}_{\text{plastic}}\|$  scales. Their  $\|\Delta \mathbf{R}_{\text{plastic}}\|$  are 2.6, 10.7, and  $47.5 \text{ \AA} \cdot (\text{g/mol})^{1/2}$  and are labeled as small-, medium-, and large-scale events, respectively. All three scale events show that the participation degree decreases with the increase of the frequency of vibrational modes, which is due to a higher energy barrier in the direction of a higher frequency mode [91]. The higher participation degree at lower frequency indicates that plastic events are mainly controlled by the low-frequency modes. To reveal the spatial characteristics of the participation modes, both  $\Delta \mathbf{R}_{\text{plastic}}$  and dominant modes of the three scale plastic events are presented in 3D real space.

For the small-scale event in Fig. 10(a), the lowest-frequency mode  $\Psi_1$  dominates the plastic event, and its participation degree is up to 0.96.  $\Delta \mathbf{R}_{\text{plastic}}$  in Fig. 11(a) shows that this event consists of a single ST with a characteristic quadrupole pattern. Particles with large magnitude of the  $\Psi_1$  polarization vectors undergo large nonaffine displacements; see Fig. 11(b). It is clearly shown that this small ST event can be predicted by the lowest-frequency mode  $\Psi_1$ .

For the medium-scale event in Fig. 10(b), both the lowest-frequency mode  $\Psi_1$  and the second-lowest frequency mode  $\Psi_2$  contribute greatly to the plastic event. Their corresponding participation degrees are 0.36 and 0.49, respectively. Interestingly, the second-lowest frequency mode  $\Psi_2$  has even larger participation ratio than the lowest one,  $\Psi_1$ . Figure 12(a) shows the total potential energy as a function of the minimization step during the energy minimization process. It is obvious that this plastic event consists of two STs: the first ST is small with a small energy drop near the 100th minimization step and the second ST is large with a large energy drop near the 200th minimization step. The two STs are separated from



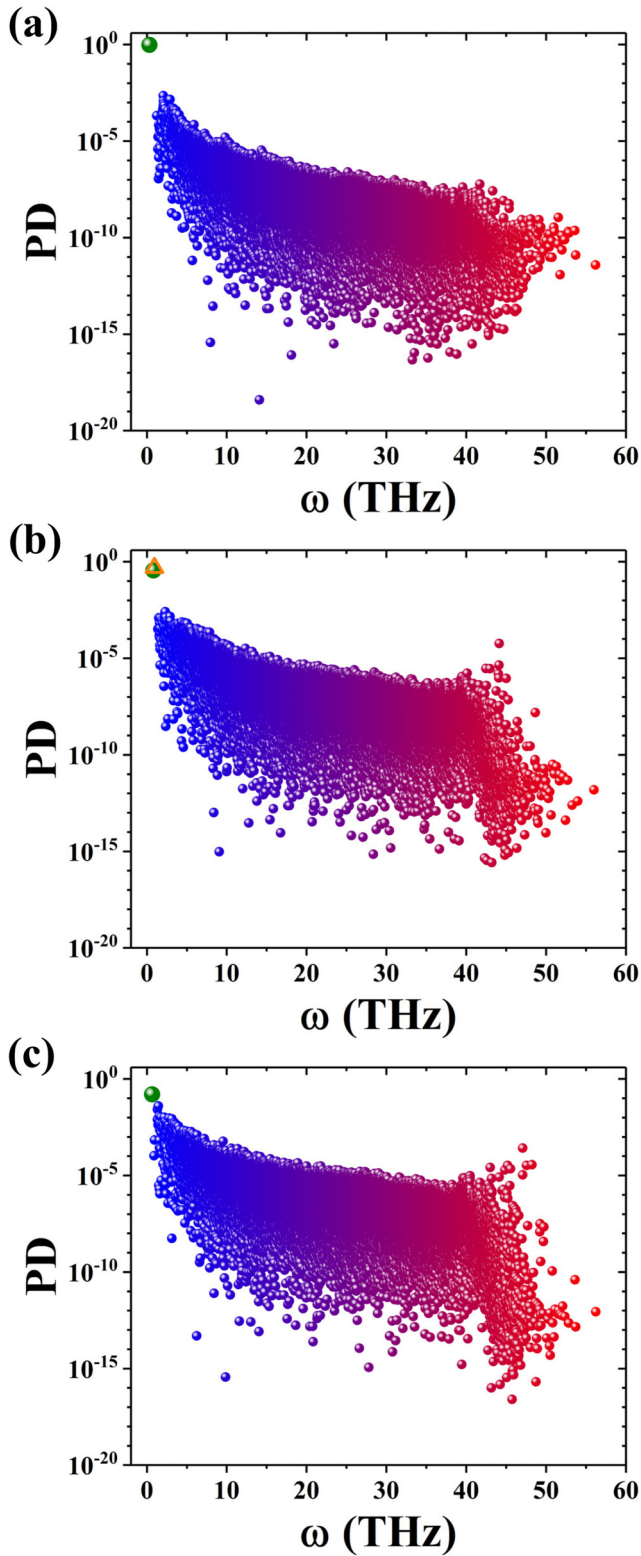


FIG. 10. Participation degree of the vibrational modes of three scale plastic events. (a)–(c) correspond to small-, medium-, and large-scale events, whose  $\|\Delta\mathbf{R}_{\text{plastic}}\|$  is 2.6, 10.7, and  $47.5 \text{ \AA} \cdot (\text{g/mol})^{1/2}$ , respectively. The green circles in (a)–(c) correspond to the lowest-frequency mode  $\Psi_1$  and the orange triangle in (b) corresponds to the second-lowest frequency mode  $\Psi_2$ .

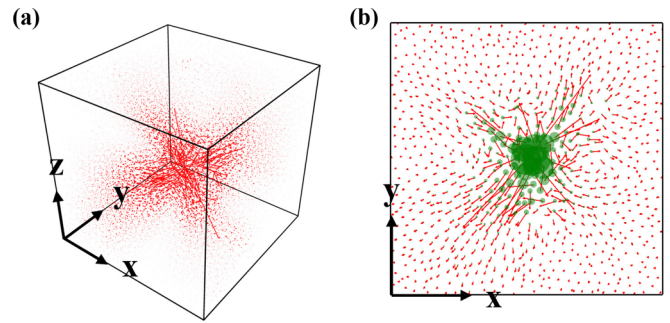


FIG. 11. Nonaffine displacement field  $\Delta\mathbf{R}_{\text{plastic}}$  of the small-scale event and its dominant vibrational mode. (a)  $\Delta\mathbf{R}_{\text{plastic}}$  of this event in 3D real space. Vector field in (b) is the slice of (a) in  $xy$  plane and the radii of green circles are proportional to the magnitude of the polarization vectors of the lowest-frequency mode  $\Psi_1$ .

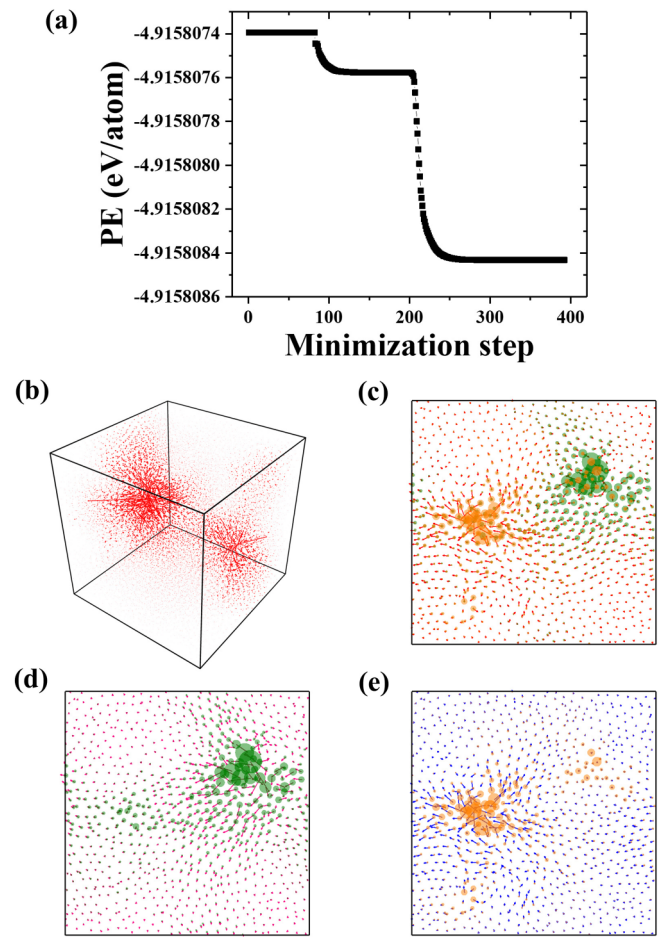


FIG. 12. Nonaffine displacement field  $\Delta\mathbf{R}_{\text{plastic}}$  of the medium-scale event and its dominant vibrational modes. (a) Plot of the total potential energy as a function of the minimization step during the energy minimization process. Two STs corresponding to the abrupt energy drops can be clearly identified. (b)  $\Delta\mathbf{R}_{\text{plastic}}$  of this event in 3D real space. Vector fields in (c)–(e) correspond to the  $xy$ -plane slice of  $\Delta\mathbf{R}_{\text{plastic}}$  of this event, the first ST, and the second ST, respectively. Radii of green circles in (c) and (d) are proportional to the magnitude of the polarization vectors of the lowest-frequency mode  $\Psi_1$ , and the radii of orange circles in (c) and (e) are proportional to the magnitude of the polarization vectors of the second-lowest frequency mode  $\Psi_2$ .

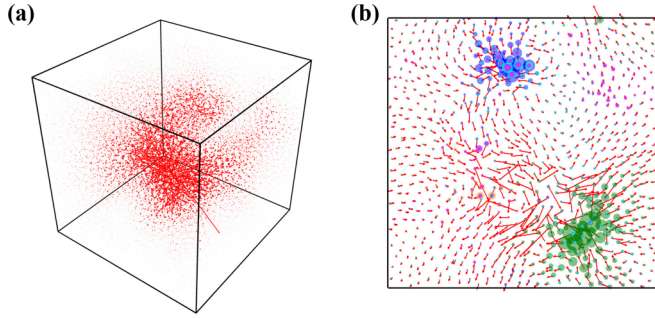


FIG. 13. Nonaffine displacement field  $\Delta\mathbf{R}_{\text{plastic}}$  of the large-scale event and its dominant vibrational modes. (a)  $\Delta\mathbf{R}_{\text{plastic}}$  of this event in 3D real space. Vector field in (b) is the slice of (a) in  $xy$  plane. Radii of green circles are proportional to the magnitude of the polarization vectors of the lowest-frequency mode  $\Psi_1$ , which has the largest participation degree. And, the radii of pink, orange, cyan, and blue circles are, respectively, proportional to the magnitude of the polarization vectors of the vibrational modes  $\Psi_7$ ,  $\Psi_4$ ,  $\Psi_{10}$ , and  $\Psi_{23}$ , which have the second-, third-, fourth-, and fifth-largest participation degree. Vibrational modes are numbered in ascending order of frequency.

each other in 3D space and can be easily distinguished by the  $\Delta\mathbf{R}_{\text{plastic}}$ ; see Fig. 12(b). The first ST indicated by  $\Psi_1$  (green circles) is on the right and the second ST indicated by  $\Psi_2$  (orange circles) is on the left; see Fig. 12(c). Because the second ST is larger than the first one, the  $\Psi_2$  mode has a larger participation degree than that of the  $\Psi_1$  mode. Thus, the most dominant mode of a plastic event, that is, the vibrational mode with the largest participation degree, may not be the critical mode that triggers the plastic event. After the first ST taking place, the elastic disturbance incurred by the first ST induces the plastic instability in the region of the second ST; see Fig. 12(d), thereby leading to the occurrence of the second ST; see Fig. 12(e). These pictures provide solid evidence for the process in which STs self-organize into avalanched plastic events by virtue of elastic interactions. In addition, it can be seen from Fig. 12(c) that both  $\Psi_1$  and  $\Psi_2$  are localized at the two STs that make up a plastic event. The entanglement of the two vibrational modes signifies that there exist strong elastic interactions between soft spots that are the candidates for plastic events, as revealed by the across-event tracing of vibrational modes [62].

For the large-scale event in Fig. 10(c), the lowest-frequency mode  $\Psi_1$  has the largest participation degree, but the value is only 0.16, comparable to some other low-

frequency modes. Figure 13(a) shows that particles with large nonaffine displacements are joined together in a system-spanning region, indicating that this plastic event consists of many correlated STs. Figure 13(b) shows that the  $\Psi_1$  mode indicates the initial ST in the lower-right corner and the subsequent STs are related to some other low-frequency modes ( $\Psi_7$ ,  $\Psi_4$ ,  $\Psi_{10}$ , and  $\Psi_{23}$ ) with the second-, third-, fourth-, and fifth-largest participation degree. The entanglement between these low-frequency modes is evidenced by observing the overlap of the localized regions of their polarization vectors. Thus, the small participation degree of the most dominant modes is due to the fact that many highly correlated STs contribute to the large-scale event and many highly entangled modes related to these STs together control such avalanched events.

From Fig. 10, there always exists a most dominant mode with the maximum participation degree:

$$PD_{\text{max}} = \max_p \{PD_p\}. \quad (18)$$

Its relation to the plastic event's scale  $\|\Delta\mathbf{R}_{\text{plastic}}\|$  is shown in Fig. 14. The decrease of  $PD_{\text{max}}$  with  $\|\Delta\mathbf{R}_{\text{plastic}}\|$  indicates that the dominant degree of a single mode decreases with the increase of the scale of plastic events. Furthermore, a critical value ( $\|\Delta\mathbf{R}_{\text{plastic}}\| \approx 10 \text{ \AA} \cdot (\text{g/mol})^{1/2}$ ) can be clearly identified. The plastic events below this critical value have a large  $PD_{\text{max}}$  with the upper boundary close to 1. The plastic events above this critical value have a small and rapidly decreasing  $PD_{\text{max}}$ . The critical value also appears in Fig. 5, which distinguishes small plastic events containing few particles from large events containing many more particles. The critical phenomenon is caused by the avalanche behavior of plastic events. Small plastic events consist of a few or even a single ST. The number of the STs contained in the plastic events increases with the increase of  $\|\Delta\mathbf{R}_{\text{plastic}}\|$ . Large plastic events occur in the form of avalanches, which consist of many STs, resulting in more particles contained in it. Therefore, more low-frequency modes with relatively low  $PD_{\text{max}}$ , associated with the STs, participate in the large events.

### B. How do plastic events influence the vibrational modes?

The influence of plastic events on vibrational modes includes two aspects: the direct influence is that plastic events alter the vibrational modes, and the indirect effect is the subsequent evolution of vibrational modes in elastic portions after events. In order to quantitatively characterize the two aspects of influence, we define a correlation matrix based on the dot product of the vibrational modes between configuration  $\mathbf{r}(\gamma')$  and configuration  $\mathbf{r}(\gamma'')$ :

$$C(\gamma', \gamma'') = \begin{bmatrix} [\Psi_1(\gamma') \cdot \Psi_1(\gamma'')]^2 & [\Psi_1(\gamma') \cdot \Psi_2(\gamma'')]^2 & \cdots & [\Psi_1(\gamma') \cdot \Psi_{3N-3}(\gamma'')]^2 \\ [\Psi_2(\gamma') \cdot \Psi_1(\gamma'')]^2 & [\Psi_2(\gamma') \cdot \Psi_2(\gamma'')]^2 & \cdots & [\Psi_2(\gamma') \cdot \Psi_{3N-3}(\gamma'')]^2 \\ \vdots & \vdots & \ddots & \vdots \\ [\Psi_{3N-3}(\gamma') \cdot \Psi_1(\gamma'')]^2 & [\Psi_{3N-3}(\gamma') \cdot \Psi_2(\gamma'')]^2 & \cdots & [\Psi_{3N-3}(\gamma') \cdot \Psi_{3N-3}(\gamma'')]^2 \end{bmatrix}, \quad (19)$$

where  $\Psi_m(\gamma')$  denotes the vibrational mode  $m$  in configuration  $\mathbf{r}(\gamma')$  and  $\Psi_n(\gamma'')$  denotes the vibrational mode  $n$  in configuration  $\mathbf{r}(\gamma'')$ . If  $\Psi_m(\gamma')$  and  $\Psi_n(\gamma'')$  correlate best with

each other, that is,

$$C_{mn}(\gamma', \gamma'') = \max_p \{C_{pn}(\gamma', \gamma'')\} = \max_q \{C_{mq}(\gamma', \gamma'')\}, \quad (20)$$

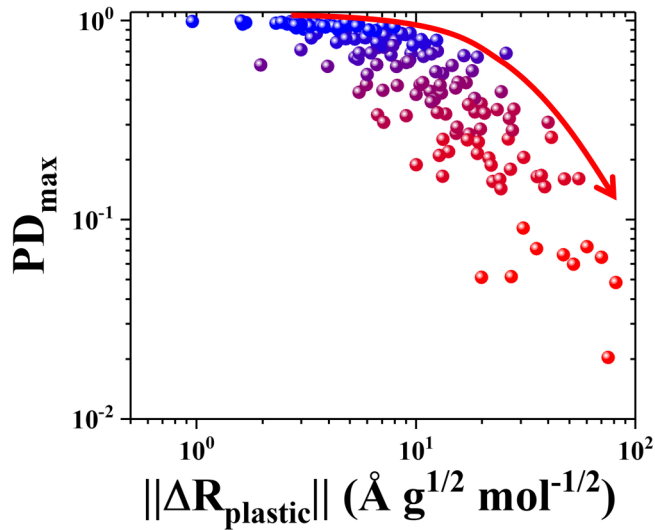


FIG. 14. Relationship between  $PD_{\max}$  and  $\|\Delta\mathbf{R}_{\text{plastic}}\|$ . Red solid arrow is drawn as a guide for the eyes.

then  $\Psi_m(\gamma')$  and  $\Psi_n(\gamma'')$  can be identified as the same vibrational mode at different deformation stages and is termed as the identifiable mode. Based on this, the identification ratio  $IR$ , defined as the ratio of identifiable modes to all vibrational modes, is used to measure the similarity of the overall vibrational modes between two configurations:

$$IR = \frac{N_{\text{idén}}}{3N - 3}, \quad (21)$$

where  $N_{\text{idén}}$  is the number of identifiable modes and  $3N - 3$  is the number of all vibrational modes excluding three Goldstone modes. A high identification ratio represents that the elasticity inheritance between two configurations is large.

Identification ratio of plastic events can be obtained by designating configurations  $\mathbf{r}(\gamma')$  and  $\mathbf{r}(\gamma'')$  as the beginning and ending strain points of plastic events, and the same is taken for elastic portions. The dependence of  $IR$  on  $\|\Delta\mathbf{R}_{\text{plastic}}\|$  and

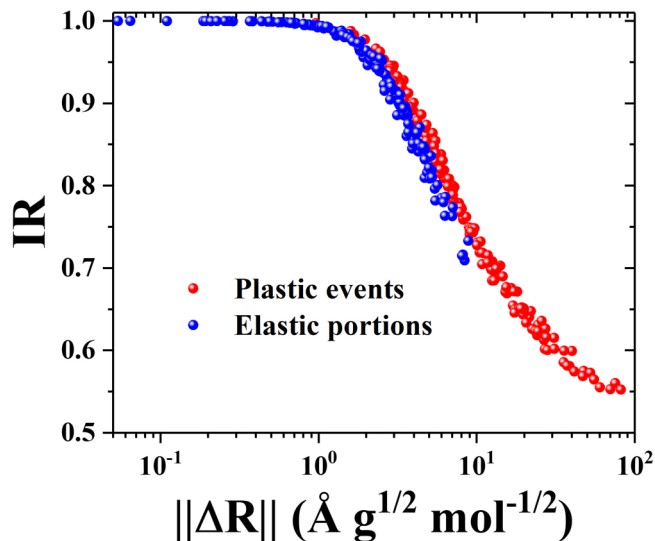


FIG. 15. Dependence of identification ratio on  $\|\Delta\mathbf{R}\|$  for elastic portions and plastic events.

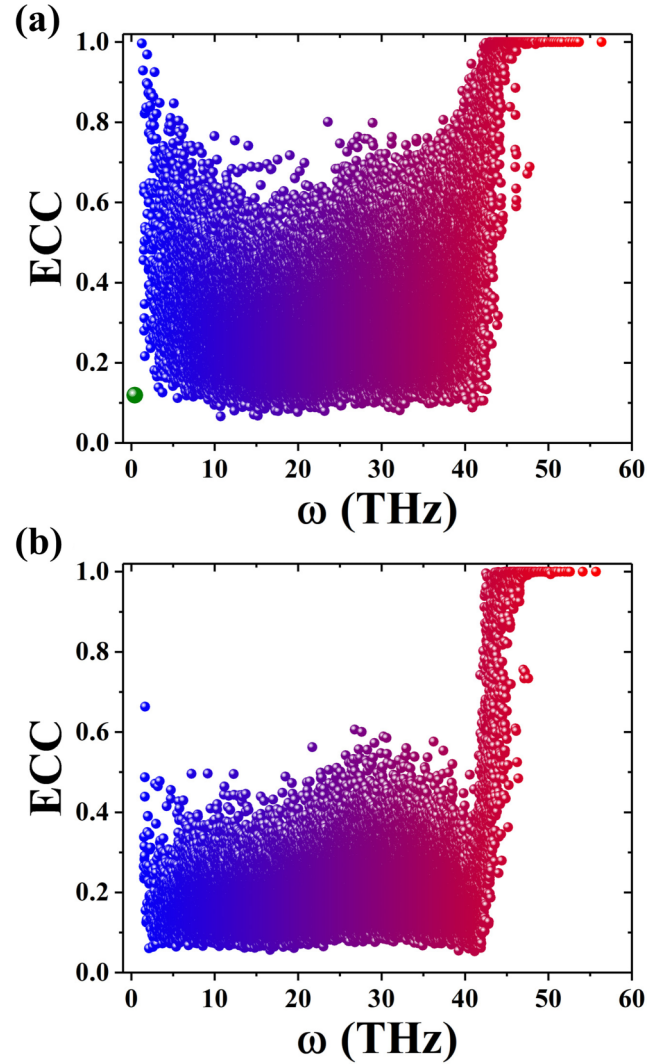


FIG. 16. Comparison of  $ECC$  between plastic event (a) and elastic portion (b) under equal  $\|\Delta\mathbf{R}\|$  of  $8.3 \text{ \AA} \cdot (\text{g/mol})^{1/2}$ . Green circle in (a) denotes  $ECC$  of the critical mode.

$\|\Delta\mathbf{R}_{\text{elastic}}\|$  is shown in Fig. 15. Identification ratio of both plastic events and elastic portions decreases with the increase of  $\|\Delta\mathbf{R}\|$ , which presents the function relation of s-shaped curve. During the loading process, elastic portions are always interrupted by plastic events. So, the  $\|\Delta\mathbf{R}\|$  of elastic portions is relatively small compared to that of plastic events, and only the first half of the s-shaped curve is observed. The decrease of identification ratio indicates that the overall vibrational modes continually evolve with either elastic or plastic deformation. A convergent and obvious function relation between  $IR$  and  $\|\Delta\mathbf{R}\|$  indicates that the identification ratio of plastic events or elastic portions is only related to the  $\|\Delta\mathbf{R}\|$ , independent of the detailed cause of it, such as the number, size, and spatial organization of the STs in the plastic events, or the loading stress level. For all studied plastic events,  $IR$  is larger than 0.5 and shows the slow decline at large  $\|\Delta\mathbf{R}\|$ . For elastic deformation,  $IR$  exceeds 0.7 and can reach about 1 at small  $\|\Delta\mathbf{R}\|$ . These results indicate that most vibrational modes can survive with the elastic deformation or even plastic events, and the destructive ability of plastic events on elasticity is limited

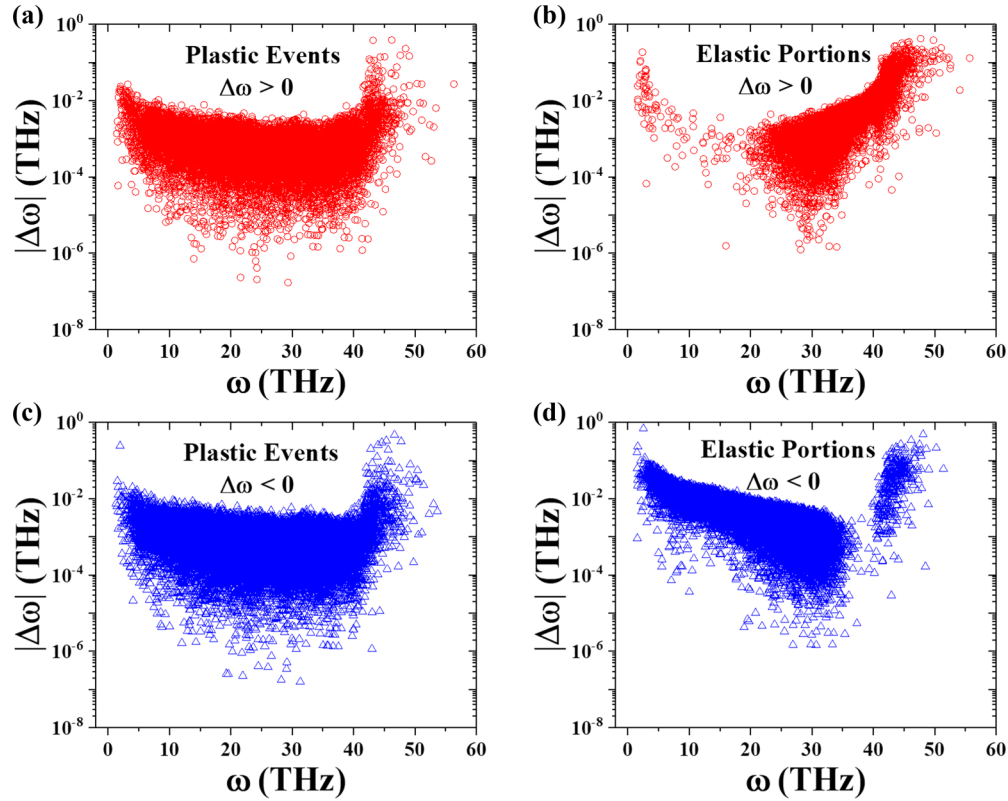


FIG. 17. Comparison of the frequency variation of identifiable modes between plastic event and elastic portion with equal  $\|\Delta\mathbf{R}\|$  of  $8.3 \text{ \AA} \cdot (\text{g/mol})^{1/2}$ ; the chosen cases are the same as that in Figs. 16(a) and 16(c) and correspond to the increase and decrease of the frequencies of plastic event, respectively. (b) and (d) correspond to the increase and decrease of the frequencies of elastic portion, respectively.

before yield. It is intriguing to observe that although the shape of these two curves is similar, the curve of elastic portions has a slight downward shift compared with that of plastic events. So, at the same  $\|\Delta\mathbf{R}\|$ , the  $IR$  in the former is smaller than that in the latter. This means that the overall vibrational modes in elastic deformation evolve more significantly than that in plastic deformation.

In the following, we explore the detailed evolution of each vibrational mode by defining the evolutionary correlation coefficient as

$$ECC_m = \max_q \{C_{mq}(\gamma', \gamma'')\}. \quad (22)$$

This coefficient denotes the correlation between the vibrational mode  $\Psi_m(\gamma')$  in configuration  $\mathbf{r}(\gamma')$  and its most relevant mode in configuration  $\mathbf{r}(\gamma'')$ . In other words, the former is most likely to evolve into the latter. A large  $ECC$  indicates a little change in the polarization vectors of the vibrational mode. Plastic event and elastic portion with equal  $\|\Delta\mathbf{R}\|$  of  $8.3 \text{ \AA} \cdot (\text{g/mol})^{1/2}$  are selected as cases for comparison and the result is shown in Fig. 16. We find that the  $ECC$  of plastic event and elastic portion is quite different. The deformation of plastic events is localized, and only parts of the soft spots are destructed, while the rest of the soft spots can be preserved. Thus, it is shown in Fig. 16(a) that the low-frequency modes corresponding to the destructed soft spots have small  $ECC$ , e.g., the critical mode. However, the low-frequency modes corresponding to the preserved soft

spots have large  $ECC$ . In contrast, the deformation of elastic portions is uniform, and the strong elastic interactions between soft spots cause the entanglement and violent evolution among the low-frequency modes, leading to small  $ECC$  of the low-frequency modes in Fig. 16(b). The polarization vectors fields of medium-frequency modes are extended and more closely related to the uniform elastic deformation. Thus, the uniform elastic deformation causes the evolution of the medium-frequency modes more significantly than the localized plastic events. This is quantitatively reflected by the smaller  $ECC$  of the medium-frequency modes in Fig. 16(b) than that in Fig. 16(a). Therefore, under the same  $\|\Delta\mathbf{R}\|$ , the identification ratio of the elastic portions smaller than that of the plastic events is caused by the larger evolution of the low- and medium-frequency modes. Besides, for both plastic events and elastic portions, the high-frequency modes are essentially unchanged, which means that the hard spots corresponding by the high-frequency modes are very robust and correspond to some stable structural units in the system, such as Cu-centered  $(0, 0, 12, 0)$  and Zr-centered  $(0, 0, 12, 4)$  Voronoi clusters [27]. These hard spots are embedded in the elastic matrix, acting as backbones to increase robustness of the elasticity.

In addition to the variation of polarization vectors as analyzed by  $ECC$  above, the evolution of the vibrational modes can also be measured by the variation of vibrational frequencies. Note that the frequency variation should be established on the identifiable modes that are considered as

the same modes during elastic deformation or plastic events. The results are shown in Fig. 17. Plastic events can cause both the increase and decrease of the vibrational frequencies [see Figs. 17(a) and 17(c)], producing random perturbation to the elasticity. It should be noted that although the polarization vectors of the high-frequency modes are essentially unchanged [Fig. 16(a)], their frequencies change greatly. This indicates that the topology of the hard spots, related to polarization vectors, remains under plastic deformation, while their hardness, related to vibrational frequencies, has changed. For elastic portions, an interesting phenomenon is discovered in Figs. 17(b) and 17(d): the frequencies of the low-frequency modes become lower and the frequencies of the high-frequency modes become higher. This means that the soft spots in the system become softer and eventually destabilize, causing plastic events to occur; meanwhile, the elastic matrix becomes stronger, enhancing the robustness of the elasticity. The elastic matrix becoming stronger is also reflected by a significant gap around 40 THz in Fig. 17(d) where the vibrational frequencies reject decline and become higher.

By the analyses of the variation of the polarization vectors and frequencies of the vibrational modes, the robust elasticity can be attributed to three factors: (i) the destruction of plastic events on elasticity is spatially limited; (ii) the hard spots embedded in elastic matrix can maintain both in the plastic events and the elastic portions; (iii) the elastic matrix gradually recovers its strength, which is diminished by the previous plastic events, during the elastic deformation. It is such robust but constant-evolving elasticity that leads to the long-standing but fast-decaying elastic interactions between plastic events.

## VII. CONCLUSION AND DISCUSSION

Our results in this paper can be summarized as follows. (i) Mediated by the robust elasticity, there are short-term strong interactions and long-term weak interactions between plastic events before yield, which lead to the plastic events belong to the correlated avalanche state. (ii) The avalanched plastic events are consistent with the fractal morphology of PEL, which suggests a transition from marginally stable state to self-organized state with mechanical loading. (iii) Clearly evidenced by the entangled low-frequency dominant modes, the picture that STs self-organized into the avalanched plastic events by virtue of elastic interactions is obtained. (iv) The robust elasticity results from the limited destructive ability of plastic events on elasticity, the hard spots acting as backbones to strengthen the elastic matrix and the self-recovery of elastic matrix during elastic deformation.

There is a great deal of work aimed at predicting plastic events, and part of it is based on vibrational modes [26,92,93]. But, their predictive ability is limited and still ongoing to improve, which can be explained by our results. The short-term strong correlation between elasticity and plasticity indicates that the short-term prediction of plastic events can be easily realized, and many works have achieved this goal even for the deterministic prediction [32,73,93]. The predictive ability diminishes as the increase of predictive range [34,36]. Thus, the long-term prediction of plastic events is challenged and

only the probabilistic prediction is achieved [26,34,92]. This is due to the long-term weak correlation between elasticity and plasticity. Nevertheless, the existence of long-term weak correlation lays the foundation for long-term prediction. By extracting key information hidden in the elasticity, sophisticated but effective machine-learning methods greatly improve the ability of long-term prediction [33,94].

Our results also provide some important insights into the construction of constitutive laws for amorphous plasticity. Avalanched plastic events before yield, acting as precursors to mechanical yielding and shear-band nucleation [21,95], are closely related to the macroscopic mechanical response of the material. The cause of the avalanches, that is, the elastoplastic interaction, is usually neglected in mean-field theory, or greatly simplified in mesoscale model [10]. It has been found that disorder-induced inhomogeneity in amorphous solids gives rise to rich phenomena in various mechanical behaviors such as yielding, shear banding, fatigue, and fracture. For many mesoscale models, only inhomogeneity of local yield threshold, described by spatially uncorrelated probability distribution, is considered, while inhomogeneity of elastic constants is usually neglected [10,20,83,96]. This leads to the deviation of elastic consequences of a pure ST from the ideal Eshelby field, as confirmed by the comparison of the deformation fields of atomistic simulations and finite-element calculations [70], which will significantly affect the avalanche behavior [97]. Thus, elastic inhomogeneity is necessary to be incorporated into the mesoscale models, including its distribution and evolution. And, they are partly reflected by our findings: the random disturbance induced by plastic events, the self-recovery in elastic deformation, and the stable hard spots.

With further mechanical loading, the system undergoes yielding transition and enters into steady flow stage finally. During the transition, the system quickly loses its stability by the destruction of stable structural units [98] and the accumulation of free volume [45,99]. Thus, the robust elasticity transforms into the transient elasticity, which is consistent with the significant increase of avalanche size and the associated fractal dimension after yield in the simulation of Lennard-Jones glass [79,80]. The transient elasticity is also evidenced by the decreasing correlation between plastic events after yield in the creep test [96].

At last, we address that the present research under AQS is still crucial even in the finite temperatures and strain rates. It can be anticipated that the introduction of thermal effect will soften the elastic matrix and reduce the interactions between plastic events, but these effects need further investigations.

## ACKNOWLEDGMENTS

This work was supported by the National Outstanding Youth Science Fund Project (Grant No. 12125206), Basic Science Center for “Multiscale Problems in Nonlinear Mechanics” (Grant No. 11988102), Major Project (Grant No. 11790292), and General Project (Grant No. 11972345) of National Natural Science Foundation of China (NSFC).

- [1] F. H. Stillinger and T. A. Weber, *Science* **225**, 983 (1984).
- [2] P. G. Debenedetti and F. H. Stillinger, *Nature (London)* **410**, 259 (2001).
- [3] P. Charbonneau, J. Kurchan, G. Parisi, P. Urbani, and F. Zamponi, *Nat. Commun.* **5**, 3725 (2014).
- [4] F. Spaepen, *Acta Metall.* **25**, 407 (1977).
- [5] A. S. Argon, *Acta Metall.* **27**, 47 (1979).
- [6] M. L. Falk and J. S. Langer, *Phys. Rev. E* **57**, 7192 (1998).
- [7] A. Furukawa and H. Tanaka, *Nat. Mater.* **8**, 601 (2009).
- [8] K. Kamrin and E. Bouchbinder, *J. Mech. Phys. Solids* **73**, 269 (2014).
- [9] E. DeGiuli, *Phys. Rev. Lett.* **121**, 118001 (2018).
- [10] A. Nicolas, E. E. Ferrero, K. Martens, and J. L. Barrat, *Rev. Mod. Phys.* **90**, 045006 (2018).
- [11] E. E. Ferrero, A. B. Kolton, and E. A. Jagla, *Phys. Rev. Mater.* **5**, 115602 (2021).
- [12] C. Maloney and A. Lemaître, *Phys. Rev. Lett.* **93**, 016001 (2004).
- [13] A. Lemaître and C. Caroli, *Phys. Rev. Lett.* **103**, 065501 (2009).
- [14] H. G. E. Hentschel, S. Karmakar, E. Lerner, and I. Procaccia, *Phys. Rev. Lett.* **104**, 025501 (2010).
- [15] S. Karmakar, E. Lerner, I. Procaccia, and J. Zylberg, *Phys. Rev. E* **82**, 031301 (2010).
- [16] S. Mandal, V. Chikkadi, B. Nienhuis, D. Raabe, P. Schall, and F. Varnik, *Phys. Rev. E* **88**, 022129 (2013).
- [17] F. Varnik, S. Mandal, V. Chikkadi, D. Denisov, P. Olsson, D. Vågberg, D. Raabe, and P. Schall, *Phys. Rev. E* **89**, 040301(R) (2014).
- [18] A. K. Dubey, H. G. E. Hentschel, I. Procaccia, and M. Singh, *Phys. Rev. B* **93**, 224204 (2016).
- [19] P. K. Jaiswal, I. Procaccia, C. Rainone, and M. Singh, *Phys. Rev. Lett.* **116**, 085501 (2016).
- [20] Z. Budrikis, D. F. Castellanos, S. Sandfeld, M. Zaiser, and S. Zapperi, *Nat. Commun.* **8**, 15928 (2017).
- [21] G. Parisi, I. Procaccia, C. Rainone, and M. Singh, *Proc. Natl. Acad. Sci. USA* **114**, 5577 (2017).
- [22] D. Şopu, A. Stukowski, M. Stoica, and S. Scudino, *Phys. Rev. Lett.* **119**, 195503 (2017).
- [23] K. Karimi, *Phys. Rev. E* **100**, 063003 (2019).
- [24] X. Xie, Y. C. Lo, Y. Tong, J. W. Qiao, G. Y. Wang, S. Ogata, H. R. Qi, K. A. Dahmen, Y. F. Gao, and P. K. Liaw, *J. Mech. Phys. Solids* **124**, 634 (2019).
- [25] X. J. Wang, Y. Z. Lu, X. Lu, J. T. Huo, Y. J. Wang, W. H. Wang, L. H. Dai, and M. Q. Jiang, *Phys. Rev. E* **105**, 045003 (2022).
- [26] M. L. Manning and A. J. Liu, *Phys. Rev. Lett.* **107**, 108302 (2011).
- [27] J. Ding, S. Patinet, M. L. Falk, Y. Cheng, and E. Ma, *Proc. Natl. Acad. Sci. USA* **111**, 14052 (2014).
- [28] J. Ding, Y. Q. Cheng, H. Sheng, M. Asta, R. O. Ritchie, and E. Ma, *Nat. Commun.* **7**, 13733 (2016).
- [29] S. Patinet, D. Vandembroucq, and M. L. Falk, *Phys. Rev. Lett.* **117**, 045501 (2016).
- [30] X. Yang, R. Liu, M. Yang, W. H. Wang, and K. Chen, *Phys. Rev. Lett.* **116**, 238003 (2016).
- [31] Y. Z. Lu, M. Q. Jiang, X. Lu, Z. X. Qin, Y. J. Huang, and J. Shen, *Phys. Rev. Appl.* **9**, 014023 (2018).
- [32] B. Xu, M. L. Falk, J. F. Li, and L. T. Kong, *Phys. Rev. Lett.* **120**, 125503 (2018).
- [33] V. Bapst, T. Keck, A. Grabska-Barwińska, C. Donner, E. D. Cubuk, S. S. Schoenholz, A. Obika, A. W. R. Nelson, T. Back, D. Hassabis, and Kohli P, *Nat. Phys.* **16**, 448 (2020).
- [34] D. Richard, M. Ozawa, S. Patinet, E. Stanifer, B. Shang, S. A. Ridout, B. Xu, G. Zhang, P. K. Morse, J.-L. Barrat, L. Berthier, M. L. Falk, P. Guan, A. J. Liu, K. Martens, S. Sastry, D. Vandembroucq, E. Lerner, and M. L. Manning, *Phys. Rev. Mater.* **4**, 113609 (2020).
- [35] M. Baggioli, I. Kriuchevskiy, T. W. Sirk, and A. Zaccone, *Phys. Rev. Lett.* **127**, 015501 (2021).
- [36] D. Ruan, S. Patinet, and M. L. Falk, *J. Mech. Phys. Solids* **158**, 104671 (2022).
- [37] S. Franz and S. Spigler, *Phys. Rev. E* **95**, 022139 (2017).
- [38] B. Shang, P. Guan, and J. L. Barrat, *Proc. Natl. Acad. Sci. USA* **117**, 86 (2020).
- [39] G. Biroli and P. Urbani, *Nat. Phys.* **12**, 1130 (2016).
- [40] S. X. Peng, C. Zhang, C. Yang, R. Li, T. Zhang, L. Liu, H. B. Yu, and K. Samwer, *J. Chem. Phys.* **150**, 111104 (2019).
- [41] C. A. Schuh and A. C. Lund, *Nat. Mater.* **2**, 449 (2003).
- [42] J. S. Harmon, M. D. Demetriou, W. L. Johnson, and K. Samwer, *Phys. Rev. Lett.* **99**, 135502 (2007).
- [43] G. P. Shrivastav, P. Chaudhuri, and J. Horbach, *Phys. Rev. E* **94**, 042605 (2016).
- [44] Y. F. Gao, B. Yang, and T. G. Nieh, *Acta Mater.* **55**, 2319 (2007).
- [45] M. Q. Jiang and L. H. Dai, *J. Mech. Phys. Solids* **57**, 1267 (2009).
- [46] A. L. Greer, Y. Q. Cheng, and E. Ma, *Mater. Sci. Eng. R* **74**, 71 (2013).
- [47] Z. Y. Yang and L. H. Dai, *Phys. Rev. Mater.* **5**, 123602 (2021).
- [48] H. G. E. Hentschel, S. Karmakar, E. Lerner, and I. Procaccia, *Phys. Rev. E* **83**, 061101 (2011).
- [49] A. K. Dubey, I. Procaccia, C. A. B. Z. Shor, and M. Singh, *Phys. Rev. Lett.* **116**, 085502 (2016).
- [50] M. Ozawa, A. Ikeda, K. Miyazaki, and W. Kob, *Phys. Rev. Lett.* **121**, 205501 (2018).
- [51] E. Bianchi, V. M. Giordano, and F. Lund, *Phys. Rev. B* **101**, 174311 (2020).
- [52] T. S. Grigera, V. Martín-Mayor, G. Parisi, and P. Verrocchio, *Nature (London)* **422**, 289 (2003).
- [53] N. Jakse, A. Nassour, and A. Pasturel, *Phys. Rev. B* **85**, 174201 (2012).
- [54] J. Yang, Y. J. Wang, E. Ma, A. Zaccone, L. H. Dai, and M. Q. Jiang, *Phys. Rev. Lett.* **122**, 015501 (2019).
- [55] H. P. Zhang, B. B. Fan, J. Q. Wu, W. H. Wang, and M. Z. Li, *Phys. Rev. Mater.* **4**, 095603 (2020).
- [56] G. Monaco and S. Mossa, *Proc. Natl. Acad. Sci. USA* **106**, 16907 (2009).
- [57] H. Mizuno, H. Shiba, and A. Ikeda, *Proc. Natl. Acad. Sci. USA* **114**, E9767 (2017).
- [58] G. Kapteijns, E. Bouchbinder, and E. Lerner, *Phys. Rev. Lett.* **121**, 055501 (2018).
- [59] L. Wang, A. Ninarello, P. Guan, L. Berthier, G. Szamel, and E. Flenner, *Nat. Commun.* **10**, 26 (2019).
- [60] D. Richard, K. González-López, G. Kapteijns, R. Pater, T. Vaknin, E. Bouchbinder, and E. Lerner, *Phys. Rev. Lett.* **125**, 085502 (2020).
- [61] P. Das and I. Procaccia, *Phys. Rev. Lett.* **126**, 085502 (2021).
- [62] J. Yang, J. Duan, Y. J. Wang, and M. Q. Jiang, *Eur. Phys. J. E* **43**, 56 (2020).

- [63] D. Wei, J. Yang, M. Q. Jiang, L. H. Dai, Y. J. Wang, J. C. Dyre, I. Douglass, and P. Harrowell, *J. Chem. Phys.* **150**, 114502 (2019).
- [64] D. Wei, J. Yang, M. Q. Jiang, B. C. Wei, Y. J. Wang, and L. H. Dai, *Phys. Rev. B* **99**, 014115 (2019).
- [65] D. Han, D. Wei, P. H. Cao, Y. J. Wang, and L. H. Dai, *Phys. Rev. B* **101**, 064205 (2020).
- [66] D. Han, D. Wei, J. Yang, H. L. Li, M. Q. Jiang, Y. J. Wang, L. H. Dai, and A. Zaccone, *Phys. Rev. B* **101**, 014113 (2020).
- [67] M. I. Mendeleev, M. J. Kramer, R. T. Ott, D. J. Sordelet, D. Yagodin, and P. Popel, *Philos. Mag.* **89**, 967 (2009).
- [68] F. Zhang, M. I. Mendeleev, Y. Zhang, C. Z. Wang, M. J. Kramer, and K. M. Ho, *Appl. Phys. Lett.* **104**, 061905 (2014).
- [69] R. Dasgupta, S. Karmakar, and I. Procaccia, *Phys. Rev. Lett.* **108**, 075701 (2012).
- [70] A. Nicolas, F. Puosi, H. Mizuno, and J. L. Barrat, *J. Mech. Phys. Solids* **78**, 333 (2015).
- [71] D. L. Malandro and D. J. Lacks, *Phys. Rev. Lett.* **81**, 5576 (1998).
- [72] C. E. Maloney and A. Lemaître, *Phys. Rev. E* **74**, 016118 (2006).
- [73] C. Maloney and A. Lemaître, *Phys. Rev. Lett.* **93**, 195501 (2004).
- [74] D. Rodney and C. Schuh, *Phys. Rev. Lett.* **102**, 235503 (2009).
- [75] S. Cui, H. Liu, and H. Peng, *Phys. Rev. E* **106**, 014607 (2022).
- [76] J. Chattoraj, C. Caroli, and A. Lemaître, *Phys. Rev. E* **84**, 011501 (2011).
- [77] P. Cao, M. P. Short, and S. Yip, *Proc. Natl. Acad. Sci. USA* **116**, 18790 (2019).
- [78] A. E. Lagogianni, C. Liu, K. Martens, and K. Samwer, *Eur. Phys. J. B* **91**, 104 (2018).
- [79] N. Oyama, H. Mizuno, and A. Ikeda, *Phys. Rev. E* **104**, 015002 (2021).
- [80] C. Ruscher and J. Rottler, *Tribol. Lett.* **69**, 64 (2021).
- [81] B. A. Sun, H. B. Yu, W. Jiao, H. Y. Bai, D. Q. Zhao, and W. H. Wang, *Phys. Rev. Lett.* **105**, 035501 (2010).
- [82] J. Antonaglia, W. J. Wright, X. Gu, R. R. Byer, T. C. Hufnagel, M. LeBlanc, J. T. Uhl, and K. A. Dahmen, *Phys. Rev. Lett.* **112**, 155501 (2014).
- [83] K. A. Dahmen, Y. Ben-Zion, and J. T. Uhl, *Phys. Rev. Lett.* **102**, 175501 (2009).
- [84] K. A. Dahmen, Y. Ben-Zion, and J. T. Uhl, *Nat. Phys.* **7**, 554 (2011).
- [85] N. P. Bailey, J. Schjøtz, A. Lemaître, and K. W. Jacobsen, *Phys. Rev. Lett.* **98**, 095501 (2007).
- [86] Y. Fan, T. Iwashita, and T. Egami, *Phys. Rev. Lett.* **115**, 045501 (2015).
- [87] V. Chikkadi, G. Wegdam, D. Bonn, B. Nienhuis, and P. Schall, *Phys. Rev. Lett.* **107**, 198303 (2011).
- [88] J. Chattoraj and A. Lemaître, *Phys. Rev. Lett.* **111**, 066001 (2013).
- [89] K. E. Jensen, D. A. Weitz, and F. Spaepen, *Phys. Rev. E* **90**, 042305 (2014).
- [90] S. Karmakar, E. Lerner, and I. Procaccia, *Phys. Rev. E* **82**, 055103(R) (2010).
- [91] N. Xu, V. Vitelli, A. J. Liu, and S. R. Nagel, *EPL* **90**, 56001 (2010).
- [92] A. Widmer-Cooper, H. Perry, P. Harrowell, and D. R. Reichman, *Nat. Phys.* **4**, 711 (2008).
- [93] L. Gartner and E. Lerner, *Phys. Rev. E* **93**, 011001(R) (2016).
- [94] E. D. Cubuk, S. S. Schoenholz, J. M. Rieser, B. D. Malone, J. Rottler, D. J. Durian, E. Kaxiras, and A. J. Liu, *Phys. Rev. Lett.* **114**, 108001 (2015).
- [95] R. Dasgupta, H. G. E. Hentschel, and I. Procaccia, *Phys. Rev. Lett.* **109**, 255502 (2012).
- [96] D. F. Castellanos and M. Zaiser, *Phys. Rev. Lett.* **121**, 125501 (2018).
- [97] A. Nicolas, J. Rottler, and J.-L. Barrat, *Eur. Phys. J. E* **37**, 50 (2014).
- [98] A. J. Cao, Y. Q. Cheng, and E. Ma, *Acta Mater.* **57**, 5146 (2009).
- [99] M. Q. Jiang, G. Wilde, and L. H. Dai, *Mech. Mater.* **81**, 72 (2015).